Photodisintegration of ^{80}Se: Implications for the *s*-process branching at ^{79}Se

A. Makinaga,[1] H. Utsunomiya,[1] S. Goriely,[2] T. Kaihori,[1] S. Goko,[3] H. Akimune,[1] T. Yamagata,[1] H. Toyokawa,[4] T. Matsumoto,[4] H. Harano,[4] H. Harada,[3] F. Kitatani,[3] Y. K. Hara,[3] S. Hohara,[5] and Y.-W. Lui[6]

[1]*Department of Physics, Konan University, Okamoto 8-9-1, Higashinada, Kobe 658-8501, Japan*

[2]*Institut d'Astronomie et d'Astrophysique, Université Libre de Bruxelles, Campus de la Plaine, CP-226, 1050 Brussels, Belgium*

[3]*Japan Atomic Energy Agency, Tokai-mura, Naka, Ibaraki 319-1195, Japan*

[4]*National Institute of Advanced Industrial Science and Technology, Tsukuba 305-8568, Japan*

[5]*Atomic Energy Research Institute, Kinki University, Kowakae 3-4-1, Osaka 577-8502, Japan*

[6]*Cyclotron Institute, Texas A&M University, College Station, Texas 77843, USA*

(Received 19 May 2008; revised manuscript received 24 November 2008; published 5 February 2009)

Photoneutron cross sections were measured for ^{80}Se immediately above the neutron separation energy with quasimonochromatic γ-ray beams to experimentally constrain the $E1$ γ strength function for ^{80}Se. Two sets of the γ strength function and the level density that equally meet the experimental constraint predict largely different neutron capture cross sections for ^{79}Se. Based on the Maxwellian-averaged cross sections of the latest compilation complemented with the predicted cross sections for ^{79}Se, we calculated σN values of the main *s*-process component using a phenomenological model and deduced empirical abundances of the weak *s*-process component. An attempt is made of considering the implications of the abundance ratios of ^{80}Kr and ^{82}Kr within the framework of phenomenological models for the weak *s* process.

DOI: 10.1103/PhysRevC.79.025801 PACS number(s): 26.50.+x, 25.20.Lj, 24.60.Dr, 27.50.+e

I. INTRODUCTION

The majority of elements heavier than the iron group nuclei are synthesized by neutron capture processes in stars, approximately a half of which are attributed to the *s* process that is slow compared to the intervening β decays [1]. Heavy elements are built up from the iron group nuclei to bismuth in the chain of neutron capture along the valley of β stability, which is terminated by the α decay of polonium-210 back to lead-206. The product of Maxwellian-averaged neutron capture cross sections (σ) at 30 keV and the solar abundances (N) plotted for the *s*-only nuclei as a function of the mass number A serves as a measure of neutron exposure to the iron group seed nuclei [2,3].

The *s*-process nucleosynthesis is classified into at least two distinct components, namely the so-called main and weak components. The main component is at the origin of heavy nuclei with $94 \leqslant A \leqslant 204$ and is believed to take place in asymptotic giant branch (AGB) stars and phenomenologically described by an exponential distribution of neutron exposures [3–5]. In contrast, the weak component is called for to explain the *s*-process production of nuclei with $A < 90$ and may be better characterized by a single neutron exposure [6,7]. The weak *s*-process nucleosynthesis is believed to take place mainly during the core He-burning phase of massive stars at neutron densities $n_n = 10^6$–10^7 cm^{-3} and temperatures around $T = 3 \times 10^8$K [8–15]. A possible reprocessing of the *s*-process matter may take place during advanced burning phases of massive stars, in particular at the bottom of the shell C-burning at a temperature $T \simeq 10^9$K and neutron density bursting from 10^9 to 10^{11} cm^{-3} on time scale of a few years [9,15–19].

The neutron capture flow includes branchings into neutron capture and β decay. The *s*-process branching takes place at radioactive nuclei with β decay rates being comparable to neutron capture rates. Attempts of analyzing some *s*-process branchings have been made to investigate the stellar condition (neutron density and temperature) associated with the main and weak components [7,20–23]. An important branching takes place at ^{79}Se [25–27]. The β-decay rate of ^{79}Se exhibits a strong temperature dependence due to thermal population of the isomeric state at 95.7 keV, potentially making ^{79}Se an *s*-process thermometer. Although experimental information on the β^- decay half-life for the isomer [20] ($\log ft = 4.70^{+0.10}_{-0.09}$) and the ground state ($T_{1/2} = 295$ ky) [28] in ^{79}Se has been improved greatly, neutron capture cross sections have remained unknown experimentally.

It is noted that the neutron capture cross section for ^{79}Se is important from the viewpoint of nuclear transmutation of the long-lived fission product, ^{79}Se, into a stable nucleus ^{80}Se [29]. Currently, a lack of a proper target sample makes a direct measurement of (n,γ) cross sections for ^{79}Se unfeasible at the n-TOF facility of CERN [30] and in the spallation neutron-beam line at J-PARC [31].

As we have done for some radioactive nuclei (^{185}W and ^{186}Re) [32], we measured photoneutron cross sections for ^{80}Se immediately above the neutron separation energy S_n to investigate the $E1$ γ strength function (γSF), which is of direct relevance for the neutron capture cross section of ^{79}Se. Experimental details are given in Sec. II. The (γ,n) data are analyzed and (n,γ) cross sections are predicted within the framework of the Hauser-Feshbach model in Sec. III. Both macroscopic and microscopic models of γSF and NLD were used in the analysis. It is shown that macroscopic and microscopic parameter sets that reproduce the (γ,n) data predict largely different (n,γ) cross sections for ^{79}Se. In Sec. IV, we discuss implications of the two different cross sections for both the main and weak *s*-process branchings at ^{79}Se. A summary is given in Sec. V.

II. EXPERIMENT AND RESULTS

Beams of quasimonochromatic γ rays were produced from laser Compton scattering (LCS) at AIST (the National Institute of Advanced Industrial Science and Technology). Laser photons from a high power Q-switch Nd:YVO_4 laser underwent head-on collisions with relativistic electrons in the storage ring TERAS (Tsukuba Electron Ring for Accelerating and Storage). The LCS γ rays were collimated into a fine beam of 2 mm diameter with a 20-cm-thick lead collimator placed at 5.5 m from the center of the interaction region of laser photons and electrons. The beams were used to irradiate a sample of 1003.3 mg ^{80}Se enriched to 99.95% that is encapsulated in a cylindrical aluminum container of 8-mm inner diameter. The maximum energy of the LCS γ-ray beam was varied from 10.00 to 10.45 MeV in the fundamental mode of the laser operation ($\lambda = 1064$ nm, 40 W) and from 10.51 to 12.71 MeV in the second harmonics ($\lambda = 532$ nm, 24 W) by changing the electron beam energy from 754.4 to 770.4 MeV and from 547.8 to 603.2 MeV, respectively. Measurements were carried out at 11 energies in the region immediately above the neutron separation energy ($S_n = 9.914$ MeV) for ^{80}Se and below S_n for Al (13.06 MeV).

Figure 1 shows a response function of a 120% high-purity germanium detector (HPGe) to an LCS γ-ray beam. Also shown in the figure is the energy distribution of the LCS beam determined in a least-squares analysis of the response function with the Monte Carlo code EGS4 [33]. The energy calibration was made with natural radioactive isotopes, ^{40}K and ^{208}Tl. The energy spread was ~0.8 MeV in the full width at half maximum, being subject to the electron beam emittance and the size of the collimator. The (γ,n) reaction was induced by a fraction of the LCS γ rays with energies above the neutron threshold (9.914 MeV). The fraction was taken into account to deduce reaction cross sections as discussed below.

The LCS γ beam was monitored with a large volume NaI(Tl) detector (8-in. diameter ×12-in. length). Figure 2 shows a measured pileup spectrum of the LCS beam along with a single-photon spectrum. The number of the LCS γ rays incident on the NaI(Tl) detector was determined by $\sum_i N_p(E_i)\,E_i/[\sum_i N_s(E_i)\,E_i/\sum_i N_s(E_i)]$. The denominator represents the average pulse height of the single photon spectrum, while the numerator represents the average pulse height of the pileup spectrum $[\sum_i N_p(E_i)\,E_i/\sum_i N_p(E_i)]$ times the total number of the γ-ray beam pulses $[\sum_i N_p(E_i)]$. Thus, the number of γ rays was determined by the product of the average number of the LCS γ rays per beam pulse and the total number of beam pulses.

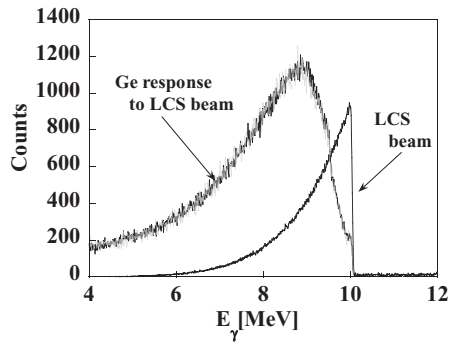

FIG. 1. A response function of a 120% high-purity Ge detector to the LCS γ-ray beam and the energy distribution of the LCS beam determined in a least-square analysis of the response function with the Monte Carlo code EGS4.

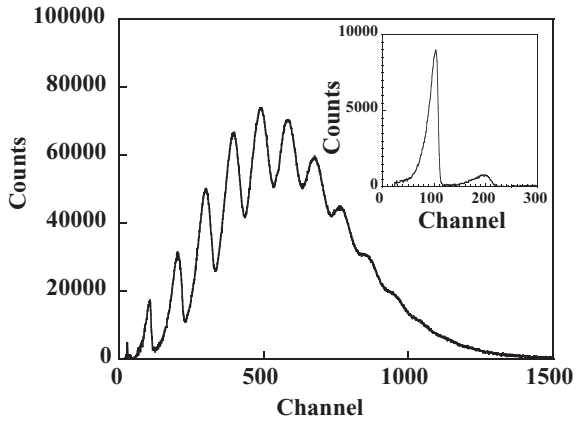

FIG. 2. Pileup and single-photon (inset) spectra of the LCS beam measured with a large volume NaI(Tl) detector measuring 8 inches in diameter and 12 inches long.

The Q-switch laser was operated at 20 kHz with a macroscopic time structure of 80 ms beam-on and 20 ms beam-off in every 100 ms. The ^{80}Se sample was mounted at the center of a 4π-type neutron detector consisting of triple rings of four (Ring 1), eight (Ring 2), and eight (Ring 3) ^{3}He proportional counters coaxially embedded in a polyethylene moderator at the distances of 3.8, 7.0, and 10.0 cm from the beam axis, respectively. Reaction and background neutrons were detected during the 80 ms beam-on, while background neutrons were detected during the 20 ms beam-off. Figures 3(a) and 3(b) show energy spectra of neutrons that were detected with the innermost Ring 1 of four ^{3}He counters during the beam-on and beam-off, respectively. Note that a low-level discriminator was set in such a way that very low energy neutrons were removed together with scattered γ-ray events. The discrimination effect was taken into account to deduce the total number of neutrons.

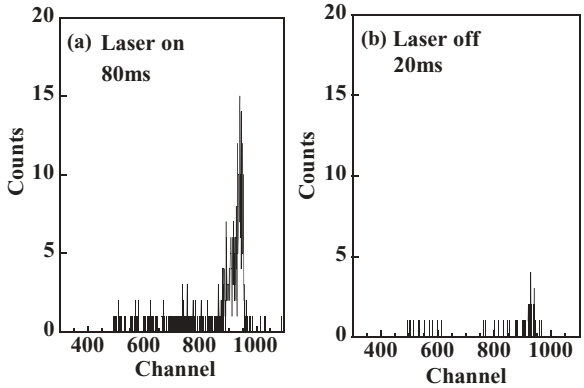

FIG. 3. Energy spectra of neutrons detected with Ring 1 of four ^{3}He counters during the 80 ms beam-on (a) and the 20 ms beam-off (b).

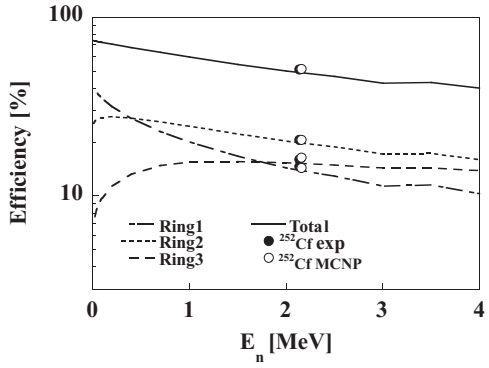

FIG. 4. Detection efficiencies of the three rings of 4 (Ring 1), 8 (Ring 2), and 8 (Ring 3) ^{3}He proportional counters coaxially embedded in the polyethylene moderator at the distances of 3.8, 7.0, and 10.0 cm from the beam axis, respectively. The efficiencies calibrated with a ^{252}Cf neutron source (solid circles) are well reproduced by MCNP Monte Carlo simulations (open circles). The neutron energy dependence of the efficiencies were obtained by the Monte Carlo simulation.

Figure 4 shows the detection efficiencies of the individual rings as well as the total efficiency. The efficiencies were calibrated with a ^{252}Cf neutron source. The results of the calibration shown by the solid circles in Fig. 4 were well reproduced by Monte Carlo simulations with the MCNP code [34] (open circles). The neutron energy dependence of the efficiencies obtained by the Monte Carlo simulation are also shown by the lines in the figure. The ring ratio technique [35] was used to determine the average neutron energies with a weighted average of three experimental ring ratios.

Photoneutron cross sections σ were determined in the monochromatic approximation of the LCS γ beams at their average energies ($E_{\rm av}$) by

$$\sigma(E_{\rm av}) = \frac{N_n}{N_\gamma\, N_t\, \epsilon_n(E_{\rm av})\, f\, g}. \qquad (1)$$

Here, N_n is the number of neutrons detected, N_γ is the number of incident LCS γ rays, ϵ_n is the neutron detection efficiency, f is a correction factor for a thick-target measurement that is given by $f = [1 - \exp(-\mu t)]/\mu t$ with the linear attenuation coefficient of γ rays μ and the target length t, and g is the fraction of the LCS γ rays above the neutron threshold that induces (γ,n) reactions. The cross sections were corrected for the energy spread of the LCS beam based on the Taylor expansion method [36]. The systematic uncertainty for the cross section is 4.5–5.3% whose breakdown is 3.2% for the neutron detection efficiency, 3% for the number of incident γ rays, and a few percentages for the time variation of the LCS beam size [36].

Results of the present photoneutron cross-section measurement for ^{80}Se are shown in Fig. 5. For comparison, the data previously obtained with continuous bremsstrahlung [37] and quasimonochromatic γ rays produced in the positron annihilation in flight [38] are also shown. We found significantly smaller cross sections near the neutron separation energy in comparison with the results of the previous measurements [37,38]. It is noted that unfolding the neutron yield curves was necessary to deduce cross sections in the former measurement, while the contribution from the positron bremsstrahlung had to be subtracted by using electron beams in the latter measurement.

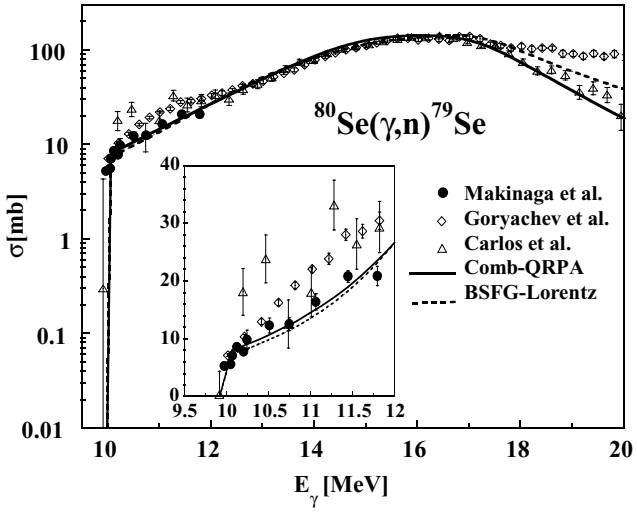

FIG. 5. Result of the present photoneutron cross section measurement for ^{80}Se in comparison with the results of the previous measurements [37,38]. The model predictions with the microscopic and macroscopic nuclear parameters of the γ strength function and the nuclear level density are also shown by the solid line and the dotted line, respectively (see text for details).

III. ANALYSIS

A. Photoneutorn cross sections

The experimental data were analyzed on the basis of a Hauser-Feshbach calculation using the TALYS code [39] and different global predictions for (i) the γ-ray strength function and (ii) the nuclear level density (NLD). For the γ-ray strength function, we consider the generalized E-dependent Lorentzian model of Ref. [40] and the Skyrme-Hartree-Fock-Bogoliubov (HFB) plus quasiparticle random phase approximation (QRPA) model of Ref. [41]. Note that in the case of the Lorentzian-type models, the $E1$ resonance energy, width, and strength at maximum are all deduced from the photoabsorption data [35]. In contrast, these quantities are predicted by the global HFB-QRPA model, and in this case, some deviations in the resonance properties could arise because no renormalization is performed. Concerning the nuclear level density two models are used, namely the back-shifted Fermi gas model (BSFG) [42] and the HFB plus combinatorial method developed by [43]. Both the strength functions and the total level densities for these models are illustrated in Fig. 6.

Two different combinations of input parameters are found to reproduce rather well the experimental photoreaction cross section. The first one (called Comb-QRPA) includes microscopic models, namely the combinatorial NLD and the HFB-QRPA strength function. The second one (called BSFG-Lorentz) uses more phenomenological (macroscopic) models, namely the BSFG model of NLD and the Lorentzian-type $E1$

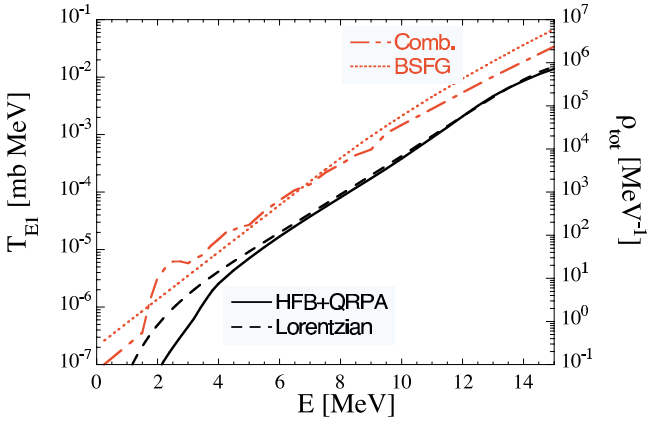

FIG. 6. (Color online) Comparison of the $E1$ transmission coefficients (left axis) and the total level density (right axis) of ^{80}Se predicted by the models adopted in the present work.

strength of Ref. [42]. The resulting comparison between the Hauser-Feshbach estimate and the available experimental data (including our new measurements) is shown in Fig. 5. Note that the photoreaction cross section is sensitive almost exclusively to the γ-ray strength function, and as seen in Fig. 6, at energies above $E = 10$ MeV, both the QRPA and the Lorentzian models give almost identical strength. The NLD only influences the cross section in a narrow energy around the neutron threshold.

B. Neutron capture cross sections for ^{79}Se

Neutron capture cross sections for ^{79}Se were predicted within the same framework of the Hauser-Feshbach model with the microscopic and the macroscopic inputs for the $E1$ γ strength function and the NLD that best reproduce the present photoneutron cross section. Figures 7(a) and 7(b) show the resulting (n,γ) cross sections and the neutron capture rate, respectively. The present capture rates with the macroscopic and microscopic parameters are larger by a factor of $\sim$1.4 and smaller by a factor of 2.4–3.6 than that of Ref. [44] in the temperature range $T_9 = 0.1$–1.0, respectively. It is of interest to see that fitting the photoneutron cross section close to the neutron threshold (Fig. 5) is a necessary condition that is not sufficient to uniquely determine the reverse reaction cross section. Indeed, the radiative neutron capture is relatively sensitive to the γ-ray strength function below the neutron threshold rather than above it. The discrepancy shown in Fig. 5 largely originates from the different energy dependences prescribed by the two different sets of models below the neutron threshold, as seen in Fig. 6. More specifically, in the energy region of interest to the radiative capture, namely the 6- to 10-MeV region, the HFB plus combinatorial total NLD is seen to lower than the BSFG prediction (note that this is even more so for the spin- and parity-dependent NLD at low energies) and the QRPA strength to be smaller than the Lorentzian one. Figure 7 therefore clearly illustrates some of the remaining model uncertainties affecting the prediction of neutron capture rates when only indirect measurements are available. The model uncertainties when no strong experimental constraints exist remain larger than the uncertainties associated with the

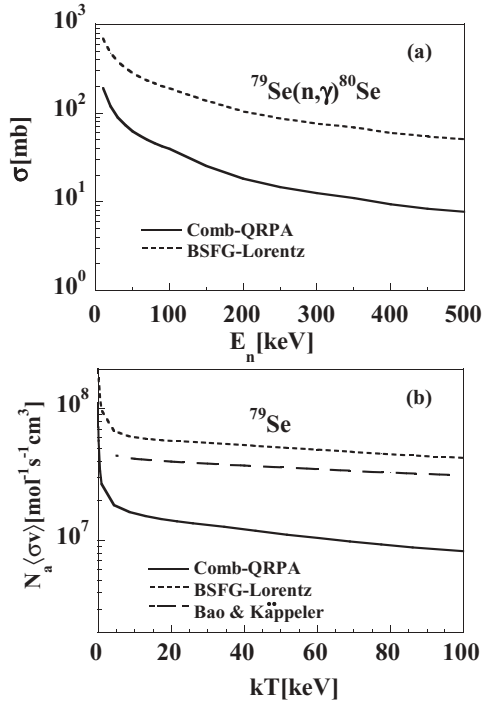

FIG. 7. Neutron capture cross sections for ^{79}Se (a) and neutron capture rates for ^{79}Se (b) predicted with the microscopic (Comb-QRPA) and macroscopic (BSFG-Lorentz) parameter sets of the γ strength function and NLD.

precise parametrization used in the corresponding models. The so-called macroscopic and microscopic sets of nuclear ingredients provide a relatively good description of the remaining errors affecting the ^{79}Se$(n,\gamma)^{80}$Se reaction rates. Note that for the stable nuclei ^{74,78,80}Se and ^{79,81}Br around $T_9 = 0.3$, both sets give rise to radiative neutron capture rates that do not differ by more than 25% and that remain within less than a factor of 2 with respect to the experimental value [44,45]. In these cases, the convergence of both sets essentially stems from NLD being constrained by s-wave spacing data at the neutron binding energy.

IV. DISCUSSIONS

Figure 8 depicts the s-process branching at ^{79}Se. Although the half-life of the ground state in ^{79}Se is sufficiently long ($T_{1/2} = 295$ ky) [28], the effective β^--decay rate is enhanced at s-process temperatures because of the thermal population of

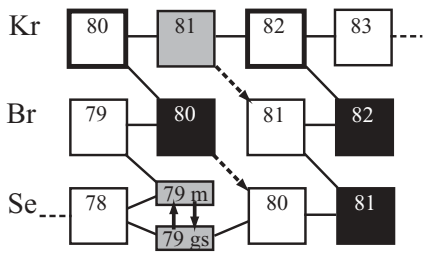

FIG. 8. s-process branching at ^{79}Se.

the isomer at 95.7 keV. The half-life for β^- decay of the isomer was experimentally determined [20]. The β^- decay branch of the s process at ^{79}Se and ^{80}Br leads to the production of the s-only nuclei ^{80}Kr and ^{82}Kr. The neutron capture branch at ^{79}Se leads to the production of ^{82}Kr by bypassing ^{80}Kr. It is noted that the EC + β^+ decays at ^{80}Br and ^{81}Kr in the β^- decay branch of ^{79}Se make additional contributions to the production of ^{82}Kr.

In this section, we discuss the effect of the two different (n,γ) cross sections deduced in Sec. III on the abundances of ^{80}Kr and ^{82}Kr resulting from branchings of the main and weak s processes at ^{79}Se and investigate their implications for the s process.

A. The main s-process component of ^{80}Kr and ^{82}Kr

The main components of s-only nuclei were calculated with the classical model [25] with an exponential distribution of neutron exposures $\rho(\tau) \propto \exp(-\tau/\tau_o)$ with $\tau_0 = 0.3$ mb^{-1} at temperature $kT = 30$ keV and the neutron density $n_n = 2.7 \times 10^8$ cm^{-3} [24]. Three kinds of Maxwellian-averaged neutron capture cross sections were employed; for all nuclei (referred to as MACS2000 hereafter) [44], complemented with the macroscopic cross section for ^{79}Se (MACRO) [44], and complemented with the microscopic cross section for ^{79}Se (MICRO) [44]. The β-decay rate was calculated at $\rho = 10^3$ g/cm^3 that is equivalent to $n_e = 3.0 \times 10^{26}$ cm^{-3} for fully ionized light elements following the prescription of Ref. [46].

The resultant σN values for the main s-process component obtained with MACRO (a) and MICRO (b) are shown in Fig. 9 by the open circles, respectively, in comparison with the empirical values based on the solar abundances of Ref. [47]. Results of the calculation are normalized to the empirical value at ^{150}Sm. The three different cross sections for ^{79}Se in MACS2000, MACRO, and MICRO result in different σN values only for nuclei with the mass number $A = 79$, 80, and 81 because the s-process flow branches at ^{79}Se and merges at ^{82}Kr. The values of σN for the main component of ^{80}Kr and ^{82}Kr are listed in Table I. The smaller the (n,γ) cross section for ^{79}Se, the larger the N for ^{80}Kr because the s-process favorably proceeds along the β^--decay branch at ^{79}Se. Although this effect is rather small between MACS2000 and MACRO, it is significantly enhanced for MICROS. The present abundances of the main component of ^{80}Kr (0.620) and ^{82}Kr (3.16) resulted from the latest compilation MACS2000 [44] are to be compared with the previous values (0.564 for ^{80}Kr and 3.38 for ^{82}Kr) given in Ref. [48].

TABLE I. The σN values of the main s-process component of ^{80}Kr and ^{82}Kr calculated with the three different sets of Maxwellian-averaged neutron captures cross sections, MACS2000[a], MACRO[b] and MICRO[c]. σ for ^{80}Kr and ^{82}Kr at 30 keV are 267±14 mb and 90±6 mb, respectively [44].

Nucleus	MACS2000[a]	MACRO[b]	MICRO[c]
^{80}Kr	166	139	231
^{82}Kr	285	285	285

[a]Maxwellian-averaged cross sections [44] for all nuclei.
[b]Maxwellian-averaged cross sections [44] complemented with the present macroscopic cross section for ^{79}Se.
[c]Maxwellian-averaged cross sections [44] complemented with the present microscopic cross section for ^{79}Se.

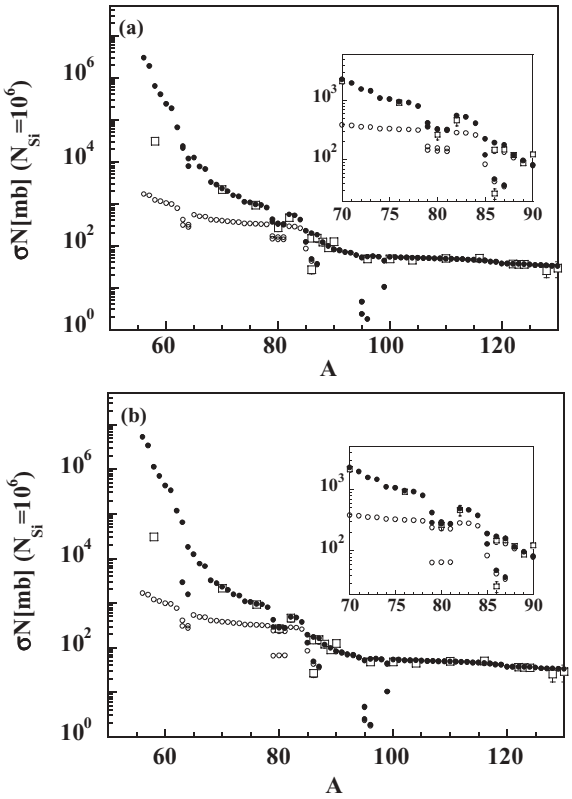

FIG. 9. σN values for the main component of the s-only nuclei (open circles) calculated with the classical model with an exponential distribution of neutron exposures $\tau_o = 0.3$ mb^{-1} using the Maxwellian-averaged cross sections of Ref. [47] complemented with the macroscopic cross section for ^{79}Se (a) and with the microscopic cross section (b) at $kT = 30$ keV and the neutron density $n_n = 2.7 \times 10^8$ cm^{-3}. For the weak component, results of the model calculations with an exponential distribution of neutron exposures $\tau_o = 0.04$ mb^{-1} at $n_n = 1.6 \times 10^8$ cm^{-3} for MACRO (a) and at $n_n = 4.5 \times 10^9$ cm^{-3} for MICRO, respectively, are shown by the filled circles on top of the main component. The empirical σN values obtained from the solar abundances of Ref. [47] and the cross sections of Ref. [44] are also shown by the open squares. The model calculation overproduces the weak abundance of ^{58}Fe.

B. The empirical weak s-process abundances of ^{80}Kr and ^{82}Kr and the weak s-process

The weak s-process abundances of ^{80}Kr and ^{82}Kr were obtained by subtracting the main components based on MACRO and MICRO from the solar isotopic abundances of Ref. [47]. Table II lists the resultant weak s-process abundances of ^{80}Kr and ^{82}Kr. The source of the uncertainty for the main s-process component lies in the solar krypton abundance and the relevant neutron capture cross section. Because the

TABLE II. The empirical weak s-process abundances of ^{80}Kr and ^{82}Kr and the abundance ratios obtained by subtracting the main component from the solar abundances.

Nucleus	MACS2000	MACRO	MICRO
^{80}Kr	0.379 ± 0.020	0.477 ± 0.025	0.135 ± 0.007
^{82}Kr	1.987 ± 0.132	1.987 ± 0.132	1.987 ± 0.132
^{80}Kr/^{82}Kr	0.191 ± 0.016	0.240 ± 0.020	0.068 ± 0.006

main component scales to the solar krypton abundance, we estimated the uncertainty of the weak abundance ratio solely from the uncertainty of σ [44], taking the relation $N \propto 1/\sigma$ into account. The abundance ratios for the weak component of ^{80}Kr and ^{82}Kr are also given in Table II.

We consider implications of the two sets of neutron capture cross sections for ^{79}Se for the weak *s* process. Note that the *p*-process contributions to the krypton abundances are not corrected for. We do not go into details of the effect of the *p*-process contribution and stay in qualitative discussions within the framework of the phenomenological models with an exponential distribution of neutron exposures [25] and with a single neutron exposure [6,7]. It is noted that a single irradiation at constant stellar temperature T and neutron density is assumed in the latter model.

The production of ^{70}Ge and ^{76}Se can be a measure of an overall reproduction of the σN curve for weak *s*-process nuclei with $A < 90$ [21]. In the exponential model, the production of ^{70}Ge and ^{76}Se is essentially determined by temperature (kT) and neutron exposure (τ_o). Given the typical stellar temperature at $kT = 26$ keV and matter density $\rho = 10^3$ g/cm^3 in the core-He burning phase of massive stars [15], the σN values of weak *s*-process ^{70}Ge and ^{76}Se are reproduced by $\tau_o \approx 0.04$, independent of neutron density. Thus, the krypton abundance ratio serves as a good measure of neutron density in the exponential model. The ratio (0.240) deduced from the macroscopic cross section is reproduced by $n_n \approx 1.6 \times 10^8$ cm^{-3} with slight overproductions of ^{80}Kr and ^{82}Kr; for instance, $N^w_{80} = 0.663$, $N^w_{82} = 2.77$, and the ratio $= 0.239$ at $\tau_o = 0.039$. In contrast, the ratio (0.068) deduced from the microscopic cross section is reproduced by $n_n \approx 4.5 \times 10^9$ cm^{-3} with proper productions of ^{80}Kr and ^{82}Kr; $N^w_{80} = 0.138$, $N^w_{82} = 2.04$, and the ratio $= 0.067$ at $\tau_o = 0.039$. The weak *s*-process abundances deduced with the Maxwellian-averaged cross section MACRO and MICRO are shown in Figs. 9(a) and 9(b) on top of the main component, respectively. It is, however, noted that the required neutron densities are higher than the typical neutron density (10^{6-7} cm^{-3}) for the core-He burning phase of massive stars. Apparently even higher neutron densities are required if the *p*-process contribution that is larger for ^{80}Kr than for ^{82}Kr is considered. It is noted that ^{58}Fe is unacceptably overproduced by the exponential model of the weak s process.

In the single exposure model, the σN values for ^{70}Ge and ^{76}Se are reproduced by $\tau \approx 0.23$ mb^{-1} at the typical stellar condition in the core-He burning phase of massive stars ($kT = 26$ keV, $n_n = 10^7$ cm^{-3}, and $\rho = 10^3$ g/cm^3). Under this condition, it was found that the ^{80}Kr/^{82}Kr ratio is

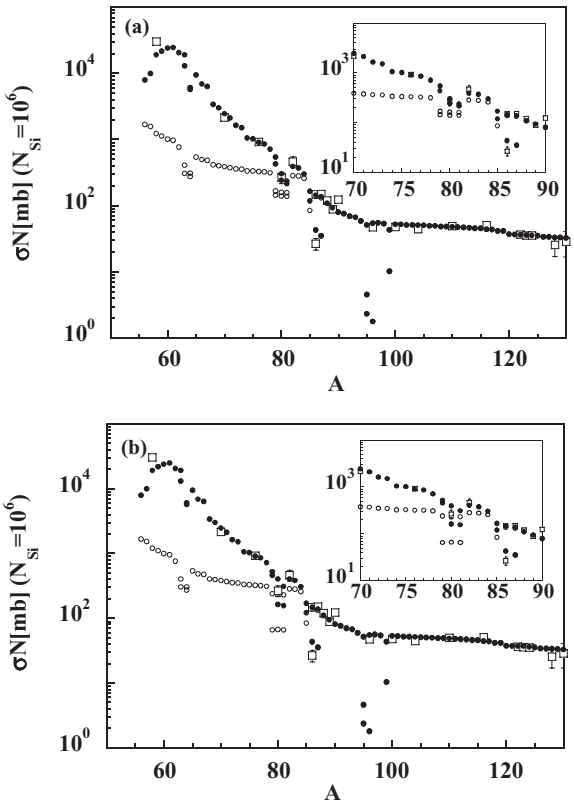

FIG. 10. σN values for the weak component (filled circles) calculated with the classical model with a single neutron exposure $\tau = 0.23$ mb^{-1} at $kT = 26$ keV, $n_n = 10^7$ cm^{-3}, and $\rho = 10^3$ g/cm^3 are shown on top of the main component for the Maxwellian-averaged cross section MACRO (a) and MICRO (b), respectively. The model calculation rather properly produces the weak abundance of ^{58}Fe. For the main component (open circles) and the empirical values (open squares); see caption of Fig. 9.

0.49–0.52, irrespective of the macroscopic and microscopic cross sections for ^{79}Se. The large ratio is mainly due to underproductions of ^{82}Kr, $N^w_{82} = 1.17$–1.10, while $N^w_{80} = 0.57$ that is compared with the empirical values of 0.477 and 0.135 for the macroscopic and microscopic cross sections for ^{79}Se. Unlike the exponential exposure distribution model, different neutron densities do not essentially change the ratio. Thus, neither of the empirical values of the weak krypton abundance ratio (0.240 and 0.068) are reproduced by using the single neutron exposure model. The σN values for the weak *s*-process component calculated with the single neutron exposure model for the Maxwellian-averaged cross sections MACRO and MICRO are shown in Figs. 10(a) and 10(b), respectively. We extended the model calculation to higher temperatures, neutron densities, and matter densities. β-decay rates were naturally extended following the prescription of the original work [46,49] and are essentially the same as those in Ref. [50]. We remark that the krypton abundance ratio deduced from the macroscopic cross section for ^{79}Se (0.24) is reproduced at $\tau = 0.45$ mb^{-1} under a stellar condition typical for the advanced shell-C burning phase of massive stars; $kT = 86$ keV, $n_n = 10^{10}$ cm^{-3}, and $\rho = 10^5$ g/cm^3. A similar observation favorable for the shell-C burning at $\tau = 0.38$ mb^{-1}

was made in Ref. [21]. However, the present neutron exposure is much larger than those averaged over the convective C shell and comparable to those at the bottom of the C shell [15].

V. SUMMARY

We measured photoneutron cross sections for ^{80}Se near the neutron separation energy to provide experimental constraints on the $E1$ γ strength function for ^{80}Se, a key nuclear parameter in the Hauser-Feshbach statistical model in calculating neutron capture cross sections for ^{79}Se. Macroscopic nuclear parameters based on the Lorentz model of the $E1$ γ-ray strength function and the back-shifted Fermi gas model of the NLD and microscopic parameters based the QRPA model of the $E1$ γ-ray strength function and the combinatorial approach of the NLD were found to equally reproduce the photoneutron cross-section data. The Hauser-Feshbach model with the macroscopic parameters predicts Maxwellian-averaged neutron capture cross sections for ^{79}Se that are larger by a factor of $\sim$1.4 at $T_9 = 0.1$–1.0 than those compiled in Ref. [44]. In contrast, the statistical model with the microscopic parameters predicts significantly smaller cross sections because of the different energy dependencies of the γ strength function and the level density below the neutron threshold. The neutron capture cross sections for ^{79}Se predicted with the microscopic nuclear parameters are smaller by a factor of 2.4–3.6 than those in Ref. [44].

We investigated implications of the macroscopic and microscopic cross sections for the s-process branching at ^{79}Se within the classical models of the main and weak s-processes. The abundances of ^{80}Kr and ^{82}Kr are very sensitive to the cross sections. The main component of ^{80}Kr and ^{82}Kr abundances was calculated in the classical model with an exponential distribution of neutron exposures and subtracted from the solar abundances to deduce the weak krypton abundances. Largely different abundance ratios for weak ^{80}Kr and ^{82}Ke resulted from the macroscopic and microscopic neutron capture cross sections for ^{79}Se. Using the weak s-process abundances, we made some qualitative considerations on stellar conditions of the weak s process within the framework of the phenomenological models. The phenomenological model analysis does not necessarily justify the stellar conditions of the core-He and the shell-C burning phases of massive stars in a stringent manner. An analysis with realistic stellar models is more desirable.

Neutron capture cross sections for ^{79}Se remain highly uncertain. Further direct or indirect efforts of determining neutron capture cross sections for ^{79}Se are needed. Indirect efforts may include a study of the γ strength function of ^{80}Se below the neutron threshold by means of the nuclear resonance fluorescence and a systematic statistical-model analysis of (γ,n) cross sections and (n,γ) cross sections for all selenium isotopes.

ACKNOWLEDGMENTS

We thank K. Takahashi for his comments on β-decay rates at high temperatures and matter densities. This work is supported by the Japan Private School Promotion Foundation and the Konan-ULB convention. S.G. acknowledges the FNRS support.

[1] E. M. Burbidge, G. R. Berbidge, W. A. Fowler, and F. Hoyle, Rev. Mod. Phys. **29**, 547 (1957).
[2] D. D. Clayton, W. A. Fowler, T. E. Hull, and B. A. Zimmerman, Annals of Physics **12**, 331 (1961).
[3] P. A. Seeger, W. A. Fowler, and D. D. Clayton, Astrophys. J. Suppl. **11**, 121 (1965).
[4] R. A. Ward, M. J. Newman, and D. D. Clayton, Astrophys. J. Suppl. **31**, 33 (1976).
[5] H. Beer, in *Proceedings of the 5th Moriond Astrophysics Meeting, Nucleosynthesis and Its Implications on Nuclear and Particle Physics*, edited by J. Audouze, N. Mathieu (Reidel, Dordrecht, 1986), p. 263.
[6] H. Beer, in *Proceedings of the 2nd IAP Rencontre on Nucl. Ap.*, edited by E. Vangioni-Flam, J. Audouze, M. Cassé, J. P. Chièze, and J. Tran Thanh Van (Editions Frontières, Paris, 1986), p. 375.
[7] H. Beer and R. L. Macklin, Astrophys. J. **339**, 962 (1989).
[8] N. Prantzos, M. Arnould, and J.-P. Arcoragi, Astrophys. J. **315**, 209 (1987).
[9] N. Langer, J.-P. Arcoragi, and M. Arnould, Astron. Astrophys. **210**, 187 (1989).
[10] N. Prantzos, M. Hashimoto, and K. Nomoto, Astron. Astrophys. **234**, 211 (1990).
[11] C. M. Raiteri *et al.*, Astrophys. J. **367**, 228 (1991).
[12] I. Baraffe, M. F. El Eid, and N. Prantzos, Astron. Astrophys. **258**, 357 (1992).
[13] L.-S. The, M. F. El Eid, and B. S. Meyer, Astrophys. J. **533**, 998 (2000).
[14] L.-S. El Eid, B. S. Meyer, and L.-S. The, Astrophys. J. **611**, 452 (2004).
[15] L.-S. The, M. F. El Eid, and B. S. Meyer, Astrophys. J. **655**, 1058 (2007).
[16] C. M. Raiteri *et al.*, Astrophys. J. **371**, 665 (1991).
[17] C. M. Raiteri *et al.*, Astrophys. J. **419**, 207 (1993).
[18] M. Limongi, O. Straniero, and A. Chieffi, Astrophys. J. Suppl. **129**, 625 (2000).
[19] S. E. Woosley, A. Heger, and T. A. Weaver, Rev. Mod. Phys. **74**, 1015 (2002).
[20] N. Klay and F. Käppeler, Phys. Rev. C **38**, 295 (1988).
[21] H. Beer, G. Walter, and F. Käppeler, Astrophys. J. **389**, 784 (1992).
[22] K. A. Toukan, K. Debus, F. Käppeler, and G. Reffo, Phys. Rev. C **51**, 1540 (1995).
[23] K. Wisshak *et al.*, Phys. Rev. C **52**, 2762 (1995).
[24] R. Reifarth *et al.*, Astrophys. J. **582**, 1251 (2003).
[25] G. Walter, H. Beer, F. Käppeler, and R.-D. Penzhorn, Astron. Astrophys. **155**, 247 (1986).
[26] G. Walter, H. Beer, F. Käppeler, G. Reffo, and F. Fabbri, Astron. Astrophys. **167**, 186 (1986).
[27] F. Käppeler, H. Beer, and K. Wisshak, Rep. Prog. Phys. **52**, 945 (1989).
[28] B. Singh, Nucl. Data Sheets **70**, 437 (1993).
[29] H. Utsunomiya *et al.*, Nucl. Phys. **A738**, 136 (2004).
[30] http://pceet075.cern.ch/ (The n_TOF Collaboration).

[31] http://j-parc.jp/MatLife/en/index.html (J-PARC Material and Life Science Facility).
[32] T. Shizuma *et al*., Phys. Rev. C **72**, 025808 (2005).
[33] W. R. Nelson, H. Hirayama, and W. O. Roger, The EGS4 Code Systems, SLAC-R-265, 1985.
[34] J. F. Briesmeister, computer code MCNP, Version 4C (Los Alamos National Laboratory, Los Alamos, 2000).
[35] B. L. Berman and S. C. Fultz, Rev. Mod. Phys. **47**, 713 (1975).
[36] H. Utsunomiya *et al*., Phys. Rev. C **74**, 025806 (2006).
[37] A. M. Goryachev, G. N. Zalensnyi, and B. A. Tulupov, Izv. Akad. Nauk SSSR, Ser. Fiz. **39**, 134 (1975).
[38] P. Carlos *et al*., Nucl. Phys. **A258**, 365 (1976).
[39] A. J. Koning, S. Hilaire, and M. C. Duijvestijn, in *Proceedings of the International Conference on Nuclear Data for Science and Technology*, edited by C. Haight *et al*. (AIP, Melville, NY, 2005), Vol. 769, p. 1154.
[40] J. Kopecky, and M. Uhl, Phys. Rev. C **41**, 1941 (1990).
[41] S. Goriely, E. Khan, and M. Samyn, Nucl. Phys. **A739**, 331 (2004).
[42] T. Belgya *et al*., *Handbook for Calculations of Nuclear Reaction Data, RIPL-2* (IAEA, Vienna, 2006).
[43] S. Hilaire and S. Goriely, Nucl. Phys. **A779**, 63 (2006).
[44] Z. Y. Bao, H. Beer, F. Käppeler, F. Voss, K. Wisshak, and T. Rauscher, At. Data Nucl. Data Tables **76**, 70 (2000).
[45] G. Rugel, I Dillman, T. Faestermann, M. Heil, F. Käppeler *et al*., Nucl. Instrum. Methods B **259**, 683 (2007).
[46] K. Takahashi and K. Yokoi, At. Data Nucl. Data Tables **36**, 375 (1987).
[47] E. Anders and N. Grevesse, Geochim. Cosmochim. Acta **53**, 197 (1989).
[48] C. Arlandini *et al*., Astrophys. J. **525**, 886 (1999).
[49] K. Takahashi (private communication).
[50] D. Neuberger (unpublished).